Numerical modelling of a segmented annular seal with enhanced lift effects

Samia Dahite, Mihai Arghir

Numerical modelling of a segmented annular seal with enhanced lift effects

Samia Dahite, Mihai Arghir

Institute PPRIME, UPR CNRS 3346, Université de Poitiers, ISAE ENSMA, France

Abstract

A segmented annular seal is composed of several identical carbon segments assembled around the rotor by a circumferential (garter) spring. Each segment has one or more pads delimited by deep grooves to generate a radial lift force when the speed of rotation is not zero. One of the solutions for enhancing this lift is to provide inclined grooves on the rotor. This solution is analyzed here numerically by assuming a thin air film between the rotor and the pad of the segment.

The thin air film is modeled by the Reynolds equation solved in a rotating coordinate system. The rotor is therefore considered fixed and the segment has an opposite speed of rotation. Due to the deep axial grooves separating the pads and the segments, the model is unsteady even in a rotating coordinate system. The approach enables the estimation of radial displacement, of the leakage rate and of the power dissipated in the seal as well as the influence of the nose friction force on the dynamic behavior of the segment. A second simplified approach neglects the axial grooves separating the pads. The modeled domain consists of a single pattern of inclined grooves with periodicity boundary conditions in the circumferential direction. This approach allows a rapid steady-state calculation that explains the opening of this kind of segmented seal.

Keywords: annular segmented seal, inclined grooves, numerical model

Introduction

The actual tendency in modern rotating machines is the replacement of traditional labyrinths with very low leakage seals [1]. These seals must have a certain compliance in order to accommodate the dynamic displacements of the rotor. The actual solutions go from full compliant brush seals to floating ring annular seals. Brush seals are very efficient in terms of leakage but operate with a continuous contact between the bristles of the brush and the rotor [2]. The leakage rate of floating ring seals is larger because they operate with a radial clearance of 10 µm to 25 µm between the rotor and the ring [3], [4]. This radial clearance remains constant for all operating conditions because the floating ring follows the radial displacements of the rotor. The segmented annular seal is a solution for drastically

diminishing the radial clearance but still preventing any contact between the rotor and the seal [3], [4]. The floating ring is therefore divided into several identical segments (Figure 1). Each segment is provided with one or several pads, a lip and a nose. The pads are delimited by deep axial grooves that separate them also from the lip.

The segments are pressed against the rotor by a garter spring while axial springs press them against the seal casing. The seal is closed at zero or very low rotor speed. With increasing rotor speed, the radial lift force generated by the pads opens the seal and prevents a premature wear. The small radial clearance following the seal opening enables a leakage flow from the high (upstream) to the low (downstream) pressure zone. The leakage flow under the lip represents the main, axial leakage path.

The nose of the seal located on the downstream face represents the secondary sealing path. The nose is permanently in contact with the seal casing and therefore this leakage path is theoretically closed. However, the contact between the nose and the casing enables a radial degree of freedom of the segment for its opening.

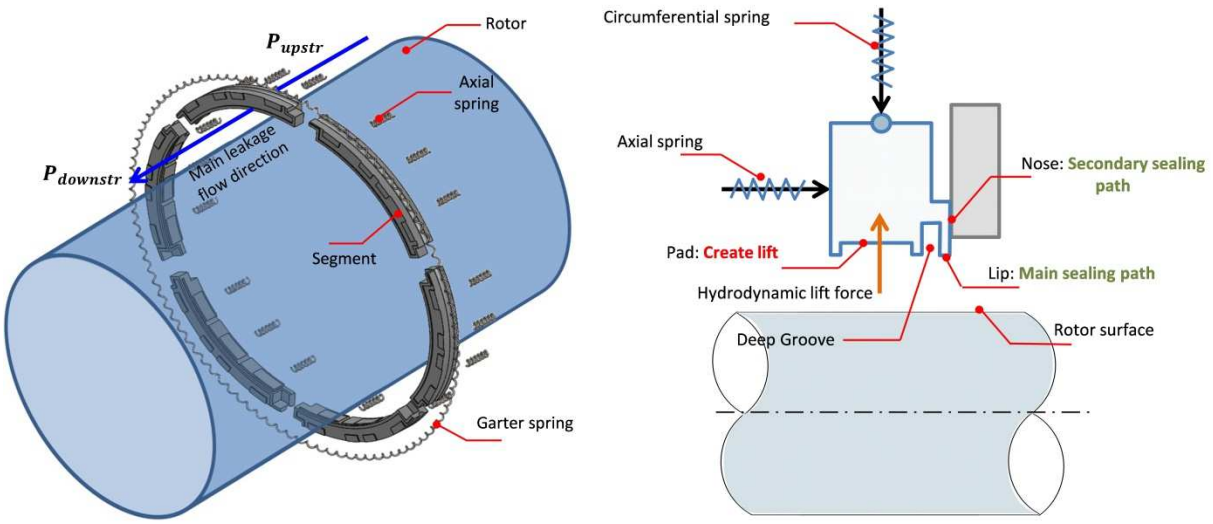

Figure 1. Annular segmented seal with pockets

The lift force that moves the segments radially and opens the seal is due to the gasodynamic pressure generated by the rotor speed and the pad. Generally, the segment has many pads that can be provided with pockets or not as in Figure 1. If the pockets are absent, the lift effects are due to the waviness errors of the pad and of the rotor. Rayleigh type pockets of constant depth and rectangular shape considerably increase the lift effects, thus avoiding contact between the segment and the rotor.

Another kind of segmented annular seal was proposed and patented by Garrison [5] in 2011. The leading feature is the use of inclined grooves manufactured on the rotor to create an enhanced lift. The design is depicted in Figure 2. The grooves are machined on the rotor surface and may have different stencils. The grooves could have been machined on the pads but the rotor solution is

preferred because the soft carbon material of the segment is prone to wear [5]. The use of several pads per segment as illustrated in Figure 1 is therefore no longer necessary. Each segment has then a single pad and circumferential groove separates the pad from the lip. The groove is continued by an axial prolongation delimiting the pad area. Inside these grooves prevails the upstream pressure. The grooves described in [5] are not only inclined but are also grouped as depicted in Figure 2. This solution might introduce a slight radial vibration of the segment that was not present in the previous designs.

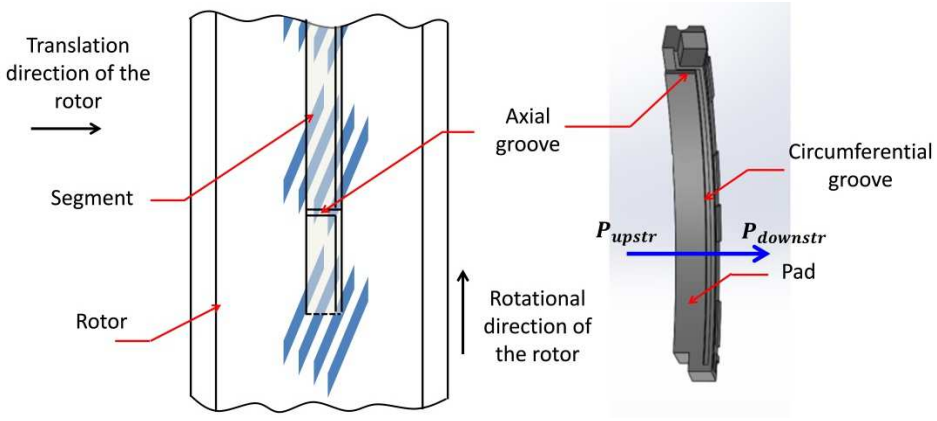

Figure 2. Annular segmented seal with enhanced lift effects

The technical and scientific literature dealing with segmented annular seals is rather scarce. Its design is described in [3] and [4] together with floating ring and face seals. Reference [3] presents also test results carried for cryogenic fluids and for operating conditions corresponding to the aerospace industry. A description of the segmented seal and details about its design is also given in [4] where almost all dynamic seals used in the aerospace industries of the '80s are discussed.

References [6] - [10] all authored by the same group of researchers present experimental results of segmented and floating ring seals tested in a cryogenic environment for the aerospace industry. The seals are tested together with a larger subcomponent of the engine and the analyses are focused on materials and surface problems, on wear and life span.

A numerical model for the annular segmented seal with pockets was presented in [11] and [12]. The model was isothermal but it was subsequently extended to non-isothermal operating conditions by coupling the rotor and segment temperature fields with the leakage flow [13], [14].

The present work is dedicated to the development of a numerical model of the segmented annular seal with a grooved rotor. This configuration is quite recent for segmented seals, but numerical models dealing with inclined grooves are present since long in the literature. The study of textured moving surfaces began with the establishment of the Narrow Groove Theory (NGT) by Whipple in 1949 [15]. This theory served for the study of smooth moving surfaces facing grooved surfaces and was mainly used for spiral and herringbone grooved thrust bearings. The NGT is based on the assumption of an infinite number of thin grooves. It introduces a reformulation of the Reynolds equation and employs a

control volume containing the discontinuity introduced by the groove. Several authors have subsequently adopted this theory and contributed to its development. Hence, Hsing [16] gave a NGT formulation considering the effects of turbulence and applied it to a viscous pump with spiral grooves. Smalley [17] presented a generalized formulation suitable for different bearing geometries. Castelli and Vohr [18] developed a model for studying the effects of large eccentricities and misalignment of a herringbone bearing while Constantinescu and Castelli [19] took into account compressibility effects in the NGT.

Several other recent studies have also adopted the NGT, a.e. [20] and [21], but others have favored a direct resolution of the Reynolds equation. The latter papers can be classified into three different categories.

The first category deals with grooves placed on the static face. They include all the studies of the spiral grooved thrust bearings and of grooved mechanical face seals. Dealing with the film discontinuity was the main challenge at the time. Wildmann [22] and Bonneau et al. [23] tackled this problem differently and came up with two kind of resolutions.

In the second category are the studies dealing with grooves on the moving surface. Normally, the unsteady character of the pressure field must be considered in the solution but the circular periodicity of the control volume considered by the NGT and the consideration of an infinite number of grooves allow a quasi-steady analysis. Bonneau and Absi [24] conducted an unsteady resolution of herringbone grooved bearings and compared it with the NGT theory while Zirkelback and San Andrés [25] calculated optimal dynamic coefficients of face seals based on the small perturbation approach.

The third category includes the analyzes of grooves on both, the fixed and moving faces. One application is the double sided spiral groove thrust bearing. For this case, Lehn and Schweizer [26] solved the Reynolds equation in the generalized case of arbitrary boundary conditions. However, they bridged the compressible and the unsteady character of the problem by considering a succession of incompressible and quasi-steady cases for different positions of the fixed and moving faces.

The present work will tackle the inclined rotor grooves by considering a rotating reference frame and two kinds of boundary conditions. For the first kind of boundary conditions that will be addressed as the general model, the unsteady character of the pressure field and of the generated lift force will be present. The unsteady character will disappear for the second kind of boundary conditions that will be addressed as the simplified model. The numerical results will show that the two models are quite equivalent.

The annular segmented seal with enhanced lift model

The geometry of the inclined grooves

For this kind of segmented seals, the radial opening force is due to the inclined grooves of the rotor that generate a lift effect as for the bearings or the face seals presented in the previous paragraph. However, as shown in Figure 2, the grooves are no longer periodic, but grouped in periodic patterns. The rotor usually carries $n_{pattern}$ equidistant stencils distributed over the entire circumference. The design of the pattern of grooves shown in [5] and in Figure 2 was somewhat simplified for the purpose of the present analysis and is depicted in Figure 3. The pattern consists of many identical grooves (i.e. of the same depth, h_{groove} and width) with the characteristic dimensions L_{xGrv} and L_{yGrv}.

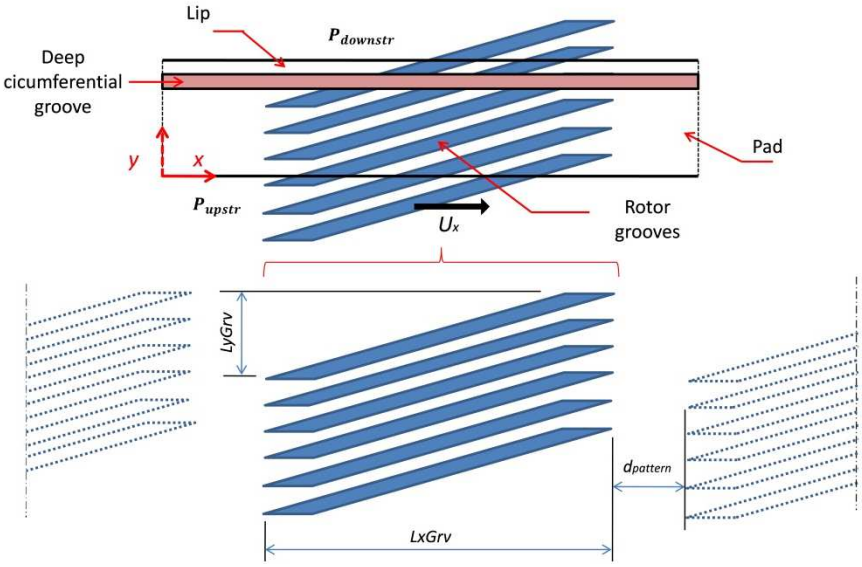

Figure 3. The groove pattern used in the present work

Figure 3 shows the grooves exceeding the upper boundary of the lip, i.e. the barrier between the large (upstream) and low (downstream) pressure zones. In usual designs, the depth of the grooves is an order of magnitude larger than the radial clearance of the seal [5]. Therefore, an important leakage rate may appear due to the pressure difference between the upstream and the downstream zones. However, the inclined grooves depicted in Figure 3 create a pumping effect acting against the pressure difference and limits the leakage flow rate.[1] This situation is shown in Figure 4. Thus, if correctly inclined, the grooves do not only contribute to lift generation, but also reduce leakage. It should be emphasized that this is not the situation described in [5] where the grooves are inclined in the opposite direction.

[1] Compared to a helical screw, the rotation would produce an axial displacement of the rotor from upstream to downstream of the seal.

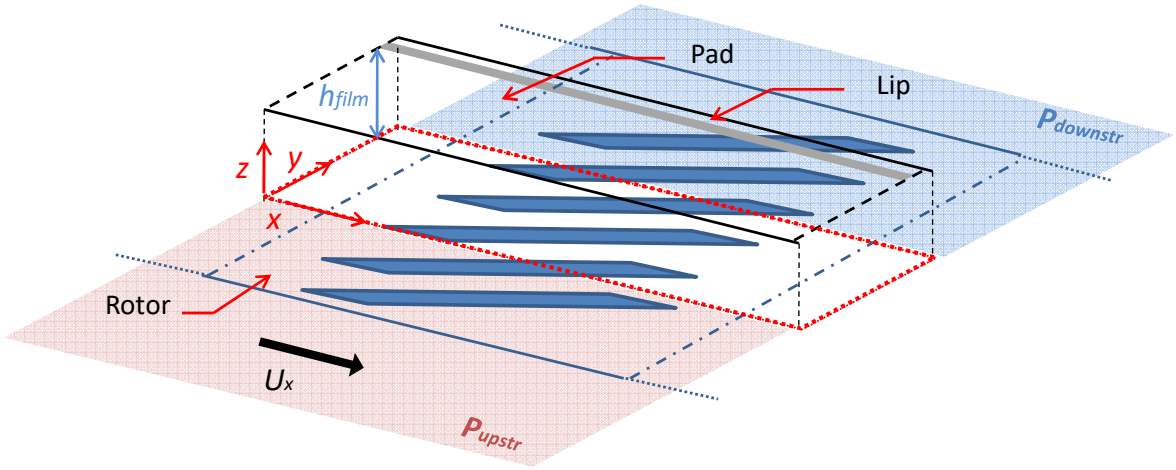

Figure 4. 3D Representation of the grooved rotor and the pad

The rotating reference frame

The spiral groove or herringbone bearings and face seals mentioned in the introduction have a large number of periodic grooves that allowed the application of the NGT. The present annular segmented seal is characterized by the periodicity of a pattern of grooves. In addition, and unlike bearings and face seals, the segmented annular seal has no circular periodicity because each segment is bordered by deep axial grooves where the upstream pressure prevails ($P_{interSeg}$ in Figure 5a).

The flow in this annular segmented seal is thus unsteady. As the numerical resolution will be carried out using the Reynolds equation, this unsteadiness would require the calculation of the derivative $\partial(Ph)/\partial t$. Due to the movement of the grooves, the time derivative of the fluid film thickness h is discontinuous in a fixed reference frame. A simpler solution is possible by considering a rotating reference frame depicted in Figure 5b. This is further explained in Figure 6 where the rotor is unwrapped.

Figure 6a depicts the movement of a grooved rotor and a fixed pad/segment. A rotating coordinate system as shown in Figure 6b overcomes the unsteady effect introduced by the rotor grooves. An observer located on the rotor would see the moving smooth surface of the pad passing by. If the seal had a circular periodicity, the flow in the rotating coordinate system would be steady. However, the deep axial grooves limiting the pads and shown in Figure 5b will be driven by a speed $-\Omega$ ($-U_x$ in Figure 6b) in the rotating system. This "artificial" displacement of the axial grooves leads to an unsteady flow even when considering a rotating reference frame. However, it will be easier to deal with the unsteady term of the Reynolds equation, $\partial(Ph)/\partial t$, because the derivative $\partial h/\partial t$ will only represent a squeeze film velocity and will be continuous.

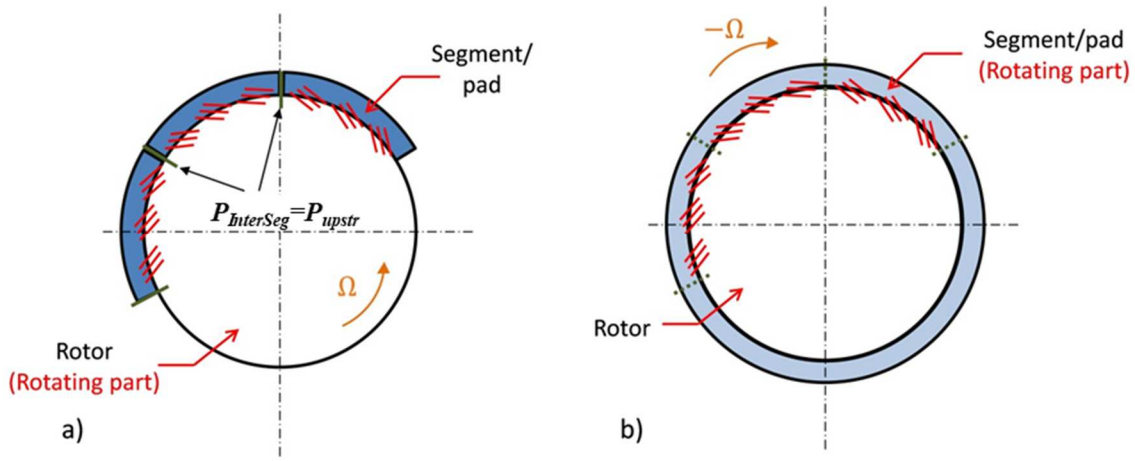

Figure 5. The segments and grooved rotor in a a) fixed reference frame, b) rotating reference frame

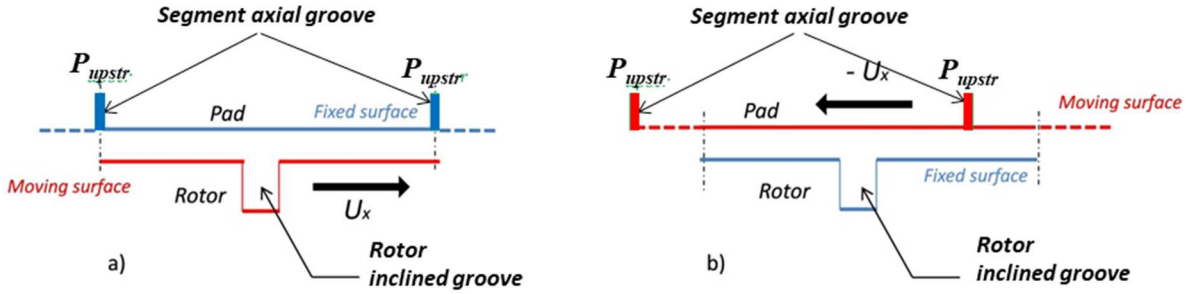

Figure 6. The unwraped rotor and a single segment in a) the fixed reference frame b) the rotating reference frame

Hence, the deep axial groove delimiting the pad and separating the segments will be modeled as a boundary with imposed pressure P_{upstr} moving with the speed $-U_x$ in the rotating coordinate system (Figure 7).

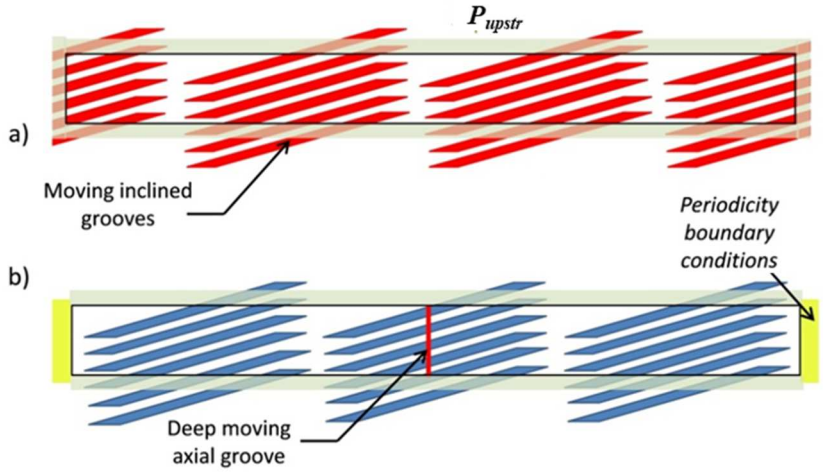

Figure 7. Representation of the pad for a) a fixed reference frame b) a rotating reference frame

The fluid film mesh

To solve the Reynolds equation, the presence of inclined grooves requires the use of an unstructured mesh. A triangular mesh was therefore employed using the software from [27] and based on the Delaunay algorithm. The pad and the lip were meshed separately. The meshing algorithm enables the discretization of the pad and of the grooves by following their boundaries as shown in Figure 8. The meshes shown in Figure 8 contain approximately 12000 and 1500 triangles for the pad and lip, respectively.

Figure 8. Mesh of the pad/segment and of the lip

Reynolds equation resolution on an triangular mesh

When it is discretized on an unstructured mesh, the Reynolds equation is more convenient to express in its divergence form:

$$\frac{\partial(\rho h)}{\partial t} + \ddot{\nabla}\vec{m} = 0 \tag{1}$$

$$\vec{m} = -\frac{\rho h^3}{12\mu}\ddot{\nabla}P + \frac{\vec{U}_I \rho h}{2} \tag{2}$$

$$\ddot{\nabla} = \frac{\partial}{\partial x}\vec{e}_x + \frac{\partial}{\partial y}\vec{e}_y, \vec{U}_I = (U_x, 0)$$

The integration over a discretization cell yields:

$$\int_S \left[\ddot{\nabla}\vec{m} + \frac{\partial(\rho h)}{\partial t}\right] dS = \oint_\Gamma \vec{m}\cdot d\vec{\gamma} + \frac{\partial(\rho h)}{\partial t} S = 0 \tag{3}$$

or:

$$\int_\Gamma \frac{\rho h^3}{12\mu}\frac{\partial P}{\partial n} d\gamma = \int_\Gamma \frac{\rho h}{2}\vec{U}_I \cdot \vec{n} d\gamma + \frac{\partial(\rho h)}{\partial t} S \tag{4}$$

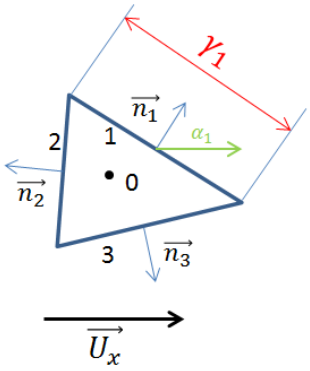

Figure 9. Triangular discretization cell

It is supposed that flow regime is isothermal and the fluid is an ideal gas governed by the state equation $P = \rho \mathcal{R} T$. The eq. (4) applied on a triangular cell depicted in Figure 9 yields:

$$\sum_{i=1}^{3} \frac{\tilde{P}_i {h_i}^3}{12\mu} \left(\frac{\partial P}{\partial n}\right)_i \gamma_i = \sum_{i=1}^{3} \frac{\tilde{P}_i h_i}{2} U_x \gamma_i \cos\alpha_i + \frac{\partial(\rho h)}{\partial t} S_0 \tag{5}$$

where $\tilde{P}$ in eq (5) are upwinded pressures needed for stabilizing the numerical solution of the Reynolds equation for large compressibility numbers:

$$\Lambda = \frac{6\mu U L}{P_{upstr} h_{min}^2} \tag{6}$$

where L and h_{min} are the two characteristic lengths of the thin film model.

For the sake of clarity and simplicity, the unsteady term of the equation $\partial(\rho h)/\partial t$ will be set aside and will be discussed later in this development.

It was shown in [12] that with the notations in Figure 10, the pressure normal derivatives over a cell face can be expressed as:

$$\left(\frac{\partial P}{\partial n}\right)_i = \frac{P_i - P_0}{l_{0i} \cos\left(\vec{n}_i, \vec{\xi}_i\right)} + \frac{P_{Bi} - P_{Ai}}{\gamma_i} \tan\left(\vec{n}_i, \vec{\xi}_i\right) \tag{7}$$

where $\cos\left(\vec{n}_i, \vec{\xi}_i\right)$ is the cosinus of the angle between the vectors $\vec{\xi}_i$ and $\vec{n}_i$ depicted in Figure 10.

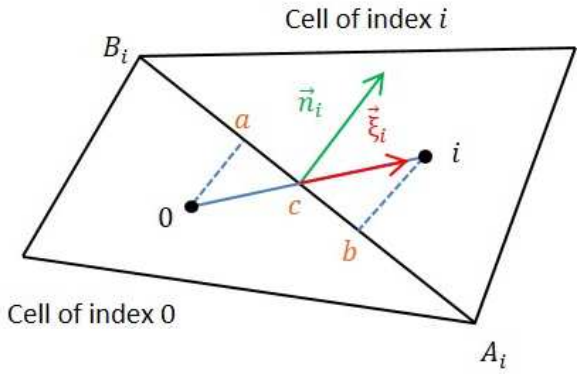

Figure 10. Notations for pressure normal derivative estimation

The pressure at a vertex of the triangular cell is estimated by averaging the pressure values in all tringles that share this common node.

$$P_{Ai} = \frac{\sum_j P_j S_j}{\sum_j S_j} \tag{8}$$

The discretized Reynolds equation for the cell pressures is then:

$$\sum_{i=1}^{3} \frac{\tilde{P}_i {h_i}^3 \gamma_i}{12\mu\, l_{0i} \cos(\vec{n}_i, \vec{\xi}_i)} P_i - \sum_{i=1}^{3} \frac{\tilde{P}_i {h_i}^3 \gamma_i}{12\mu\, l_{0i} \cos(\vec{n}_i, \vec{\xi}_i)} P_0 = \sum_{i=1}^{3} \tilde{P}_i \frac{h_i}{2} U_x \gamma_i \cos\alpha_i - \sum_{i=1}^{3} \tilde{P}_i \frac{{h_i}^3}{12\mu} (P_{Bi} - P_{Ai}) \tan(\vec{n}_i, \vec{\xi}_i) \tag{9}$$

The upwind pressures in eqs. (5) and (9) are calculated by using the pressures in two triangles and the sign of the normal velocity on the common face. For example, with the notations employed in Figure 10.

$$\tilde{P}_i = P_0 \delta_i + P_i (1 - \delta_i) \qquad \delta_i = \frac{1 + sign(V_{ni})}{2} \tag{10}$$

where the normal velocity on the common face is:

$$V_{ni} = \vec{V}_i . \vec{n}_i = \frac{\dot{m}_{ni}}{\rho_i h_i} == \frac{-{h_i}^2}{12\mu} \left(\frac{\partial P}{\partial n}\right)_i + \frac{U_x}{2} \cos\alpha_i \tag{11}$$

Equation (9) is then nonlinear due to the presence of the upwind pressures. However, another strong non-linearity is introduced when thin film discontinuities introduced by grooves must be considered. This situation is illustrated in Figure 11.

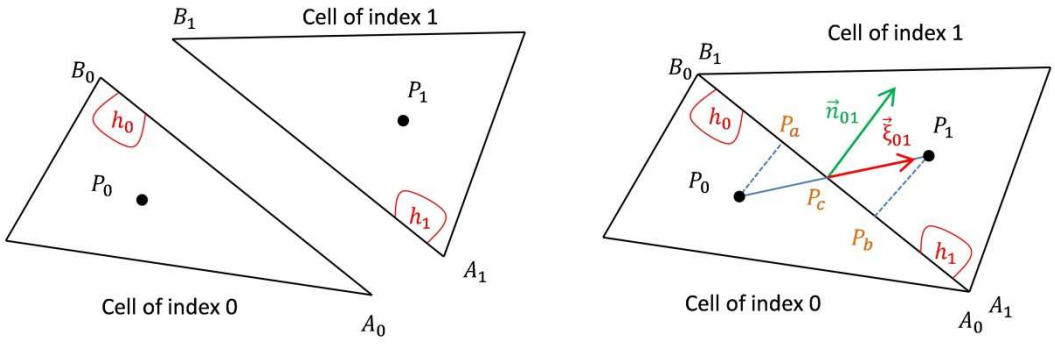

Figure 11. Cells and notations for considering the thin film discontinuity

The thin film thickness on the face A_0B_0 belonging to the cell of subscript "0" is h_0 while it is h_1 on the face A_1B_1 of the cell "1". It is supposed that the pressure values between the two discretization cells are continuous but not the pressure derivatives. This means:

$$P_{B_0} = P_{B_1} = P_B \qquad P_{A_0} = P_{A_1} = P_A \tag{12}$$

and $l_{A_0B_0} = l_{A_1B_1} = l_{AB}$. The problem when the pressure derivatives are discontinuous is the loss of mass conservation. Therefore, this must be reinforced.

The mass fluxes across the common face AB expressed in the two triangles are:

$$\dot{m}_{n0,1} = -\frac{\rho_{0,1}{h_0}^3}{12\mu}\left(\frac{\partial P}{\partial n}\right)_{0,1} + \frac{\rho_{0,1}h_0}{2}\vec{U}_x\cdot\vec{n}_{0,1} \tag{13}$$

$$\dot{m}_{n1,0} = -\frac{\rho_{1,0}{h_1}^3}{12\mu}\left(\frac{\partial P}{\partial n}\right)_{1,0} + \frac{\rho_{1,0}h_1}{2}\vec{U}_x\cdot\vec{n}_{1,0} \tag{14}$$

The pressure normal derivatives are:

$$\left(\frac{\partial P}{\partial n}\right)_{0,1} = \frac{P_a - P_0}{l_{0a}} = \frac{P_a - P_0}{l_{0c}\cos(\vec{n},\vec{\xi})} \tag{15}$$

$$\left(\frac{\partial P}{\partial n}\right)_{1,0} = \frac{P_b - P_1}{l_{1b}} = \frac{P_b - P_1}{l_{1c}\cos(\vec{n},\vec{\xi})} \tag{16}$$

The pressures P_a and P_b on the face AB are approximated as it follows:

$$P_a = P_c + \frac{P_B - P_A}{l_{AB}} l_{ca} = P_c + \frac{P_B - P_A}{l_{AB}} l_{0c} \sin\left(\vec{n}_{01}, \vec{\xi}_{01}\right) \tag{17}$$

$$P_b = P_c - \frac{P_B - P_A}{l_{AB}} l_{cb} = P_c - \frac{P_B - P_A}{l_{AB}} l_{1c} \sin\left(\vec{n}_{01}, \vec{\xi}_{01}\right) \tag{18}$$

Following these approximations, the pressure normal derivatives are:

$$\left(\frac{\partial P}{\partial n}\right)_{0,1} = \frac{P_c - P_0}{l_{0c} \cos\left(\vec{n}, \vec{\xi}\right)} + \frac{P_B - P_A}{l_{AB}} \tan\left(\vec{n}, \vec{\xi}\right) \tag{19}$$

$$\left(\frac{\partial P}{\partial n}\right)_{1,0} = \frac{P_c - P_1}{l_{1c} \cos\left(\vec{n}, \vec{\xi}\right)} + \frac{P_A - P_B}{l_{AB}} \tan\left(\vec{n}, \vec{\xi}\right) \tag{20}$$

The pressures at the cell centers P_0 and P_1 are unknown while the pressures at the cell vertexes P_A and P_B are interpolated using eq. (8). The pressure P_c is expressed by enforcing the conservation of the mass fluxes across the face AB:

$$\dot{m}_{n0,1} + \dot{m}_{n1,0} = 0 \tag{21}$$

Injecting eqs. (13) , (14) and eqs (19) , (20) in eq. (21) yields

$$P_c = \frac{{h_1}^3 - {h_0}^3}{12\mu(C_1 + C_0)} \frac{P_B - P_A}{l_{AB}} \tan\left(\vec{n}, \vec{\xi}\right) + \frac{h_0 - h_1}{2(C_1 + C_0)} U_x \cos\alpha + \frac{C_0 P_0 + C_1 P_1}{C_1 + C_0} \tag{22}$$

$$C_0 = \frac{{h_0}^3}{12\mu\, l_{0c} \cos\left(\vec{n}, \vec{\xi}\right)} \qquad C_1 = \frac{{h_1}^3}{12\mu\, l_{1c} \cos\left(\vec{n}, \vec{\xi}\right)} \tag{23}$$

The pressure normal derivative in cell “0” is then

$$\left(\frac{\partial P}{\partial n}\right)_{0,1} = \frac{P_B - P_A}{l_{AB}} \tan\left(\vec{n}, \vec{\xi}\right) \tag{24}$$
$$+ \frac{1}{l_{0c} \cos\left(\vec{n}, \vec{\xi}\right)} \left[\frac{{h_1}^3 - {h_0}^3}{12\mu(C_1 + C_0)} \frac{P_B - P_A}{l_{AB}} \tan\left(\vec{n}, \vec{\xi}\right) + \frac{h_0 - h_1}{2(C_1 + C_0)} U_x \cos\alpha + \frac{C_1}{C_1 + C_0} (P_1 - P_0) \right]$$

It can be observed that when the thin film discontinuity is absent, i.e. $h_0 = h_1$, this yields eq. (7).

A system of discretized equations different from (9) is obtained when the pressure normal derivatives (24) are used in the Reynolds equation integrated over a triangular cell (5). This system writes:

$$\sum_{i=1}^{3} a_i P_i - a_0 P_0 = b_0 \tag{25}$$

$$a_i = \frac{\tilde{P}_i {h_{0i}}^3 \gamma_i}{12\mu\, l_{0c_i} \cos\left(\vec{n}_i, \vec{\xi}_i\right)} \frac{C_{ii}}{C_{ii} + C_{0i}} \qquad a_0 = \sum_{i=1}^{3} a_i \tag{26}$$

$$C_{ii} = \frac{{h_{ii}}^3}{12\mu\, l_{ic_i} \cos\left(\vec{n}_i, \vec{\xi}_i\right)} \qquad C_{0i} = \frac{{h_{0i}}^3}{12\mu\, l_{0c_i} \cos\left(\vec{n}_i, \vec{\xi}_i\right)} \tag{27}$$

$$\begin{aligned} b_0 = & \sum_{i=1}^{3} \tilde{P}_i \frac{h_{0i}}{2} U_x \gamma_i \cos\alpha_i \\ & - \sum_{i=1}^{3} \tilde{P}_i \frac{{h_{0i}}^3}{12\mu} (P_{Bi} - P_{Ai}) \tan\left(\vec{n}_i, \vec{\xi}_i\right) \left[1 + \frac{1}{l_{0c_i} \cos\left(\vec{n}_i, \vec{\xi}_i\right)} \frac{{h_{ii}}^3 - {h_{0i}}^3}{12\mu(C_{ii} + C_{0i})}\right] \\ & - \sum_{i=1}^{3} \tilde{P}_i \frac{{h_{0i}}^3}{12\mu} \gamma_i \frac{h_{0i} - h_{ii}}{2(C_{ii} + C_{0i})} \frac{U_x \cos\alpha_i}{l_{0c_i} \cos\left(\vec{n}_i, \vec{\xi}_i\right)} \end{aligned} \tag{28}$$

The system of eqs. (25) can be written in a more compact form

$$[A(P)]\{P\} = \{B(P)\} \tag{29}$$

underlining its nonlinear character. The numerical solution of the system of eqs. (29) is obtained by using a Newton algorithm. The residues of eqs. (29) are:

$$R(P) = \sum_{i=1}^{3} a_i P_i - a_0 P_0 - b_0 \tag{30}$$

and the iterative solution following the Newton-Raphson algorithm is:

$$\{P\}^{(k+1)} = \{P\}^{(k)} - \left[\left(\frac{\partial R}{\partial P}\right)^{(k)}\right]^{-1} \{R\}^{(k)} \tag{31}$$

However, the practice showed that this is not sufficient for obtaining convergence when the non-linearity in eq. (25) or (29) is very strong, a.e. in the case of deep groves. This is due to the vertex

pressures P_A and P_B of the term b_0 given by eq. (28). The stencil coupling the pressures around cell "0" consists not only of the pressures in the cells "1", "2" and "3" that share a common face (Figure 12a) but of all the pressures that share a common vertex. This situation is depicted in Figure 12b.

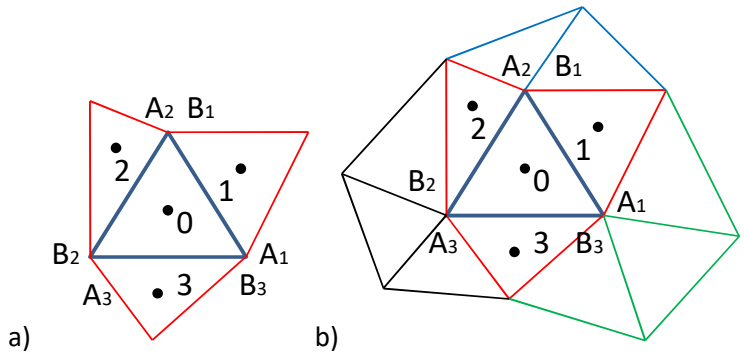

Figure 12. The stencil of the coupled pressures, simplified (a) and complete (b)

The pressure P_A and P_B of the right hand side term b_0 are moved on the left hand side of eq. (25) and yield a modified discretized equation.

$$\sum_{i=1}^{3}(a_i+\bar{a}_i)P_i+\sum_{i=1}^{3}\sum_{j_{B_i}=1\backslash\{i\}}^{n_{B_i}}\bar{a}_{j_{B_i}}P_{j_{B_i}}-\sum_{i=1}^{3}\sum_{j_{A_i}=1\backslash\{i\}}^{n_{A_i}}\bar{a}_{j_{A_i}}P_{j_{A_i}}-(a_0+\bar{a}_0)P_0=\bar{b}_0 \tag{32}$$

The additional terms are:

$$\bar{a}_i=\varphi_i S_i\left(\frac{1}{\sum_{k_{B_i}=0}^{n_{B_i}}S_{k_{B_i}}}-\frac{1}{\sum_{k_{A_i}=0}^{n_{A_i}}S_{k_{A_i}}}\right) \tag{33}$$

$$\bar{a}_0=\sum_{i=1}^{3}\varphi_i S_0\left(\frac{1}{\sum_{k_{B_i}=0}^{n_{B_i}}S_{k_{B_i}}}-\frac{1}{\sum_{k_{A_i}=0}^{n_{A_i}}S_{k_{A_i}}}\right) \tag{34}$$

$$\varphi_i=\widetilde{P}_i\frac{{h_{0i}}^3}{12\mu}\tan\left(\vec{n}_i,\vec{\xi}_i\right)\left[1+\frac{1}{l_{0c_i}\cos\left(\vec{n}_i,\vec{\xi}_i\right)}\frac{{h_{ii}}^3-{h_{0i}}^3}{12\mu(C_{ii}+C_{0i})}\right] \tag{35}$$

$$\bar{a}_{j_{B_i}}=\frac{\varphi_i S_{j_{B_i}}}{\sum_{k_{B_i}=0}^{n_{B_i}}S_{k_{B_i}}}\qquad\bar{a}_{j_{A_i}}=\frac{\varphi_i S_{j_{A_i}}}{\sum_{k_{A_i}=0}^{n_{A_i}}S_{k_{A_i}}} \tag{36}$$

$$\bar{b}_0=\sum_{i=1}^{3}\widetilde{P}_i\frac{h_{0i}}{2}U_x\gamma_i\cos\alpha_i-\sum_{i=1}^{3}\widetilde{P}_i\frac{{h_{0i}}^3}{12\mu}\gamma_i\frac{h_{0i}-h_{ii}}{2(C_{ii}+C_{0i})}\frac{U_x\cos\alpha_i}{l_{0c_i}\cos\left(\vec{n}_i,\vec{\xi}_i\right)} \tag{37}$$

where n_{A_i} and n_{B_i} are the numbers of triangles sharing A_i or B_i as a common vertex.

The residues given by eq. (30) are also modified.

$$\bar{R}(P) = \sum_{i=1}^{3}(a_i + \bar{a}_i)P_i + \sum_{i=1}^{3}\sum_{j_{B_i}=1\backslash\{i\}}^{n_{B_i}} \bar{a}_{j_{B_i}} P_{j_{B_i}} - \sum_{i=1}^{3}\sum_{j_{A_i}=1\backslash\{i\}}^{n_{A_i}} \bar{a}_{j_{A_i}} P_{j_{A_i}} - (a_0 + \bar{a}_0)P_0 - \bar{b}_0 \qquad (38)$$

The terms of the Jacobian matrix $[\partial \bar{R}/\partial P]$ are given in the Appendix.

Equation (38) is fully implicit and therefore the Newton-Raphson algorithm is robust. The computational speed is enhanced by employing sparse matrix storage and the algorithm from reference [28] for solving the linear system in eq. (31).

For the unsteady Reynolds equation, the terms a_0 and b_0 of equations (25)-(30), and then (32)-(38) will include the contribution of $[\partial(\rho h)/\partial t]_0 \, S_0$:

$$\bar{a}'_0 = \bar{a}_0 + \left[\frac{{h_0}^{(n)}}{\Delta t} + \left(\frac{\partial h}{\partial t}\right)_0^{(n)}\right] S_0 \qquad \bar{b}'_0 = \bar{b}_0 - \frac{{P_0}^{(n-1)}{h_0}^{(n)}}{\Delta t} S_0 \qquad (39)$$

where all the elements of the equations will be at the instant (n) except the terms of the previous calculation time indexed with $(n-1)$.

Results

The main characteristics of the seal (leakage flow rate and dissipated power) can be estimated when the segment opening is known. In the general case, the segment has three degrees of freedom (two displacements and one rotation) because the nose slides against the flat surface of the stator as shown in Figure 1. However, it was shown in [11], [13] and [14] that the radial displacements is dominant. This displacement is depicted as e_X on Figure 13 and it is a key parameter of the segmented seal because it explains its opening. However, taking into account only the radial displacement of the segment e_X and discarding its lateral displacement e_Y and its rotation should be considered as an approximation of the analysis.

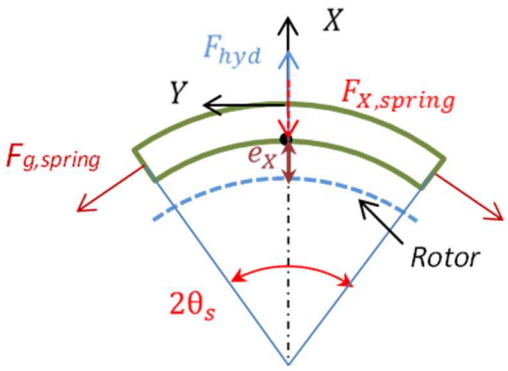

Figure 13. Forces applied on the segment

Hence, the surfaces of the rotor and of the pad are considered parallel and the fluid film thickness is:

$$h_{filmP} = e_X + \delta_P h_{groove} \text{ with } \delta_P = \begin{cases} 1 \text{ , } if\ P \in Groove \\ 0 \text{ , } if\ P \notin Groove \end{cases} \quad (40)$$

where P identifies the center of a discretization cell. This approximation is consistent with considering only the radial degree of freedom of the segment. Moreover, parallel pad and rotor surfaces is a requirement for using the periodicity boundary conditions shown in Figure 7b.

General approach

The general approach considers the presence of the axial grooves limiting each pad and their movement in the rotating reference frame as shown in Figure 6. Each segment is provided with a single pad. The length of the pad will therefore be equal to the length of the segment, $L_{xPad} = L_{xSeg}$. The pressure P_{upstr} depicted in Figure 6 prevails inside the deep axial grooves delimiting the segments. Periodicity boundary conditions will be considered on the circumferential edges of the computational domain as shown in Figure 7b while the pressure P_{upstr} will be imposed on the top and bottom boundaries and on a cross section of small width corresponding to the deep axial groove.

For comparison, Figure 14a depicts the grid and the pressure generated in the pad without any axial groove while Figure 14b depicts the same results for the case of an axial groove modeled as an internal zone of very small width carrying an imposed constant pressure. The width of the internal zone is limited to one column of triangular cells.

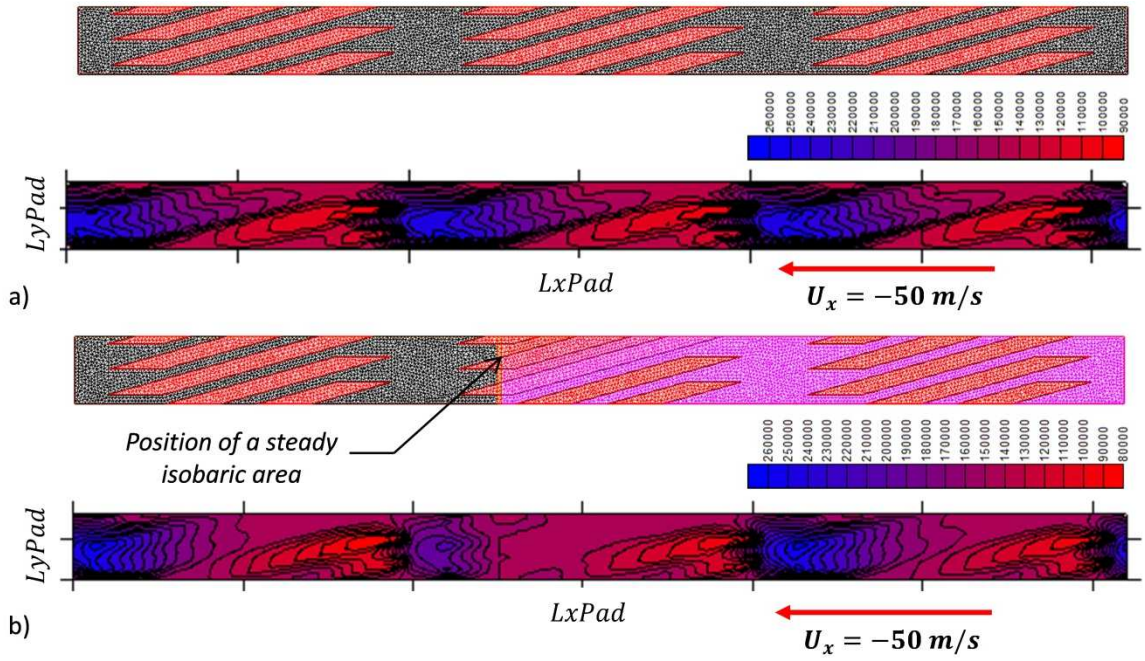

Figure 14. Pad pressure field for a radial displacement $e_X = 4\ \mu m$ a) without any axial groove b) with an axial groove modeled as an internal boundary with constant pressure

These results show how the pressure field is modified by the presence of the constant pressure axial groove. In Figure 14a, the lift generated without the axial groove is $F_{hyd} = 13{,}6\ N$ while it is $F_{hyd} = 6{,}9\ N$ for case in Figure 14b. The lift force would be different for another position of the internal zone with constant pressure; thus, an unsteady lift effect is generated when the axial groove moves along the pad. At each time step, the constant pressure zone moves by the distance $-U_x \Delta t$ and therefore a new mesh is generated. An interpolation of the pressures calculated at the instant $(n-1)$ is performed over the mesh of the instant (n).

The results of the unsteady calculations for two imposed radial displacements, $e_X = 4\ \mu m$ and $e_X = 2\ \mu m$ are presented in Figure 15. The time step is $\Delta t = 10^{-5}\ s$, the number of mesh elements is approximately $20\ 000$ triangles and the speed is $U_x = -50\ m/s$. The upstream/downstream pressure difference is $\Delta P = 0{,}5\ bar$. The hydrodynamic force oscillates around an average value, $F_{avrg} \cong 9\ N$ and $F_{avrg} \cong 32\ N$, for the two imposed radial displacements. An oscillation period corresponds to the time required by the constant pressure zone to move through a single pattern of grooves.

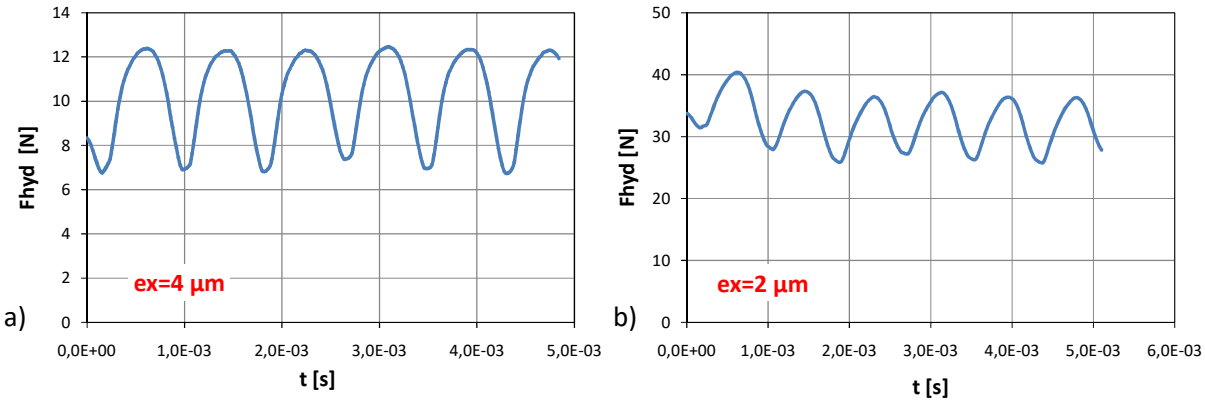

Figure 15. Time variation of the hydrodynamic lift force of the pad (*Δt=10⁻⁵ s* , mesh density=20000 trgs and *U_x=-50 m/s*) for an imposed film thickness of a) *e_x=4 µm* b) *e_x=2 µm*

The accuracy of the numerical results was verified by performing several calculations with different time steps and at two different grid densities. The results for a radial displacement $e_X = 4\ \mu m$ are presented in Figure 16 and show minor variations with the time step and the grid density. The results of the following paragraph are therefore obtained with $\Delta t = 10^{-5}\ s$ and a mesh of $2{\cdot}10^4$ triangles.

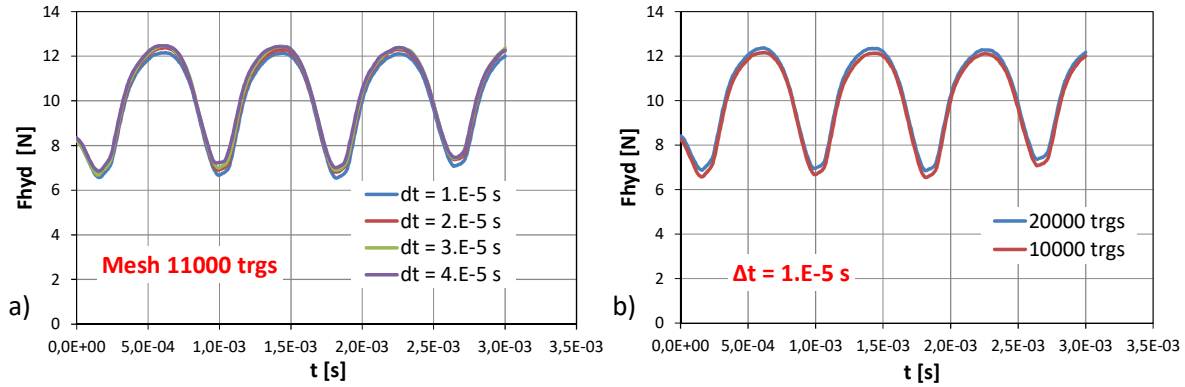

Figure 16. Accuracy of the numerical results with the time step and the grid density (*e_x=4 µm*)

Imposed radial load; the e.o.m. of the segment with 1 d.o.f.

The general case, when the radial load is imposed by the garter spring requires the numerical time integration of the equation of motion of the segment with 1 d.o.f. The pad sector will be subjected to three types of loads: hydrodynamic, elastic and the nose friction forces.

$$M\ddot{e}_X = F_{hyd}(e_X, \dot{e}_X) - F_{X,spring} - F_{f,nose}sign(\dot{e}_X) \tag{41}$$

The pressures of the pad and of the lip generate the hydrodynamic force.

$$F_{hyd} = F_{n,fluid\_p} + F_{n,fluid\_l} \tag{42}$$

The radial force applied by the circumferential spring is:

$$F_{X,spring} = 2 \sin \theta_s \, F_{g,spring} \tag{43}$$

where θ_s is the half amplitude of the pad sector.

The friction force on the nose $F_{f,nose}$ is:

$$F_{f,nose} = F_{f,fluid} + F_{f,asp} \approx F_{f,asp} = f_{eq} F_Z \tag{44}$$

and its detailed calculation considering mixed lubrication conditions under the nose is given in [11].

Due to the presence of the unsteady friction force, this equation is integrated using the explicit 1st order Euler method:

$$\begin{cases} \ddot{e}_X{}^{(n)} = \dfrac{1}{M}\left[F_{hyd}{}^{(n-1)}(e_X, \dot{e}_X) - F_{X,spring} - F_{f,nose}{}^{(n-1)} sign(\dot{e}_X)\right] \\ \dot{e}_X{}^{(n)} = \dot{e}_X{}^{(n-1)} + \ddot{e}_X{}^{(n)} \, \Delta t \\ e_X{}^{(n)} = e_X{}^{(n-1)} + \dfrac{\Delta t}{2}\left[\dot{e}_X{}^{(n)} + \dot{e}_X{}^{(n-1)}\right] \end{cases} \tag{45}$$

The nose Coulomb friction force (44) is calculated by the penalty method.

$$F_{f,nose} = K_t (e_X - e_{X_0}) \tag{46}$$

Following this model, the friction force is induced by the elastic deformation of the asperities of stiffness, K_t. However, the discontinuities induced when the velocity $\dot{e}_X$ changes sign must be smoothed for enabling the numerical integration. This is performed by adopting the following approximation [29] :

$$F_{f,nose}{}^{(n)} = \begin{cases} K_t\left(e_X{}^{(n)} - e_X{}^{(n-1)}\right), if \ \left|F_{f,nose}\right| < f_{eq} F_Z \\ f_{eq} F_Z \dfrac{2}{\pi} \arctan\left[C_t\left(e_X{}^{(n)} - e_X{}^{(n-1)}\right)\right], otherwise \end{cases} \tag{47}$$

The model reproduces “stick-slip” effects and takes into account the history of the motion of the segment.

The following results are obtained with and without the nose friction force, for an axial spring force, $F_{Z,spring} = 5N$, a pressure difference, $\Delta P = 0.5\ bar$ and a mass of the segment, $M = 50\ g$.

Figure 17 presents the results obtained for a linear speed $U_x = -50\ m/s$ and a radial force applied by the garter spring, $F_{X,spring} = 5\ N$. The displacement amplitudes without the nose friction force are more important. This is due to the damping brought by the Coulomb friction force. The average value of the radial displacement is $e_X = 5{,}3\ \mu m$ and the amplitudes do not exceed $0{,}6\ \mu m$ without friction and $0{,}2\ \mu m$ with friction. The hydrodynamic force oscillates around the value of the garter spring radial force and the average leakage mass flow rate of the seal is $Q_m = 0{,}3\ g/s$. The average value of the seal power loss is $\mathcal{P}_r = 42\ W$.

The garter spring was kept constant during dynamic calculations because the diameter of the segmented seal is close to 200 mm and the radial displacements are many orders of magnitudes smaller. The variation of the length of the garter spring due to the radial displacement of the segment is therefore negligible.

Figure 18 shows that the nose friction force varies between two limits $\pm f_{eq} F_Z = \pm\ 1{,}3\ N$ alternating between stick and slip zones. The segment is in the stick mode most of the time and the slip zones correspond to the time intervals when the constant pressure narrow zone moves between two consecutive patterns. They correspond also to the local minima and maxima of the radial displacements. The period of the radial displacements corresponds to the time required for constant pressure zone to cross a complete pattern and is $T = 8{,}27 \cdot\ 10^{-4} s$.

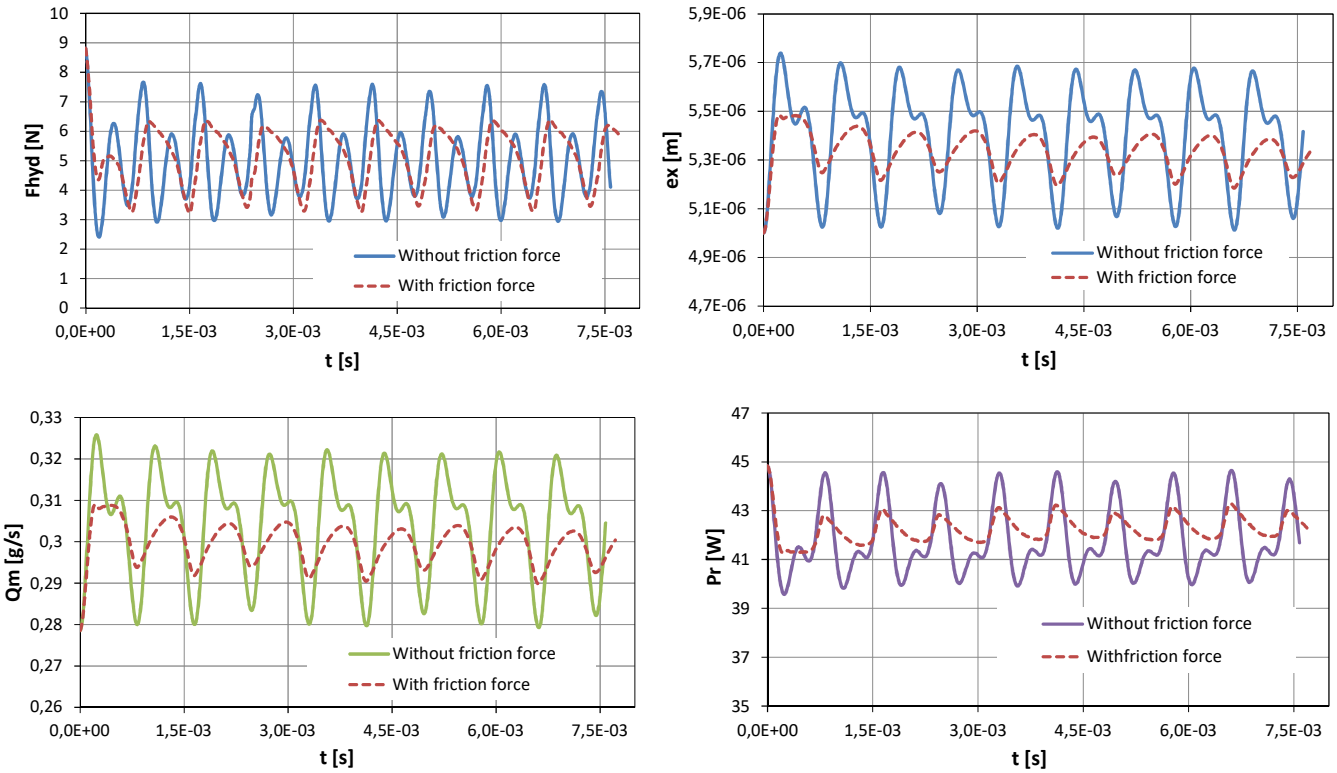

Figure 17. Results of the 1 d.o.f. dynamic analysis for $F_{X,spring} = 5N$ and $U_x = -50\ m/s$

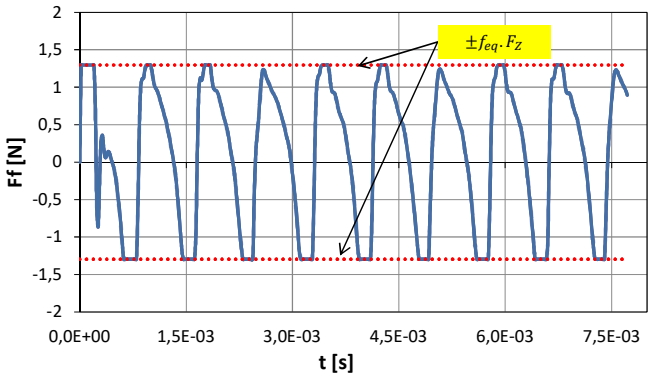

Figure 18. Variation of the nose friction force for $F_{X,spring} = 5N$ and $U_x = -50\ m/s$

Figure 19 and Figure 20 show the results for the same value of the linear speed, $U_x = -50\ m/s$, but a larger garter spring force, $F_{X,spring} = 10\ N$. The displacements are smaller than for the previous case with an average value, $e_x = 3{,}9\ \mu m$. The amplitudes with and without friction are much closer and go from $0{,}3\ \mu m$ to $0{,}5\ \mu m$. The average leakage mass flow rate and power loss are $Q_m = 0{,}22\ g/s$ and $\mathcal{P}_r = 53\ W$. The period of the radial displacements is the same as in the previous case but the "slip" zones depicted in Figure 20 are much more pronounced and are spread over a larger time interval.

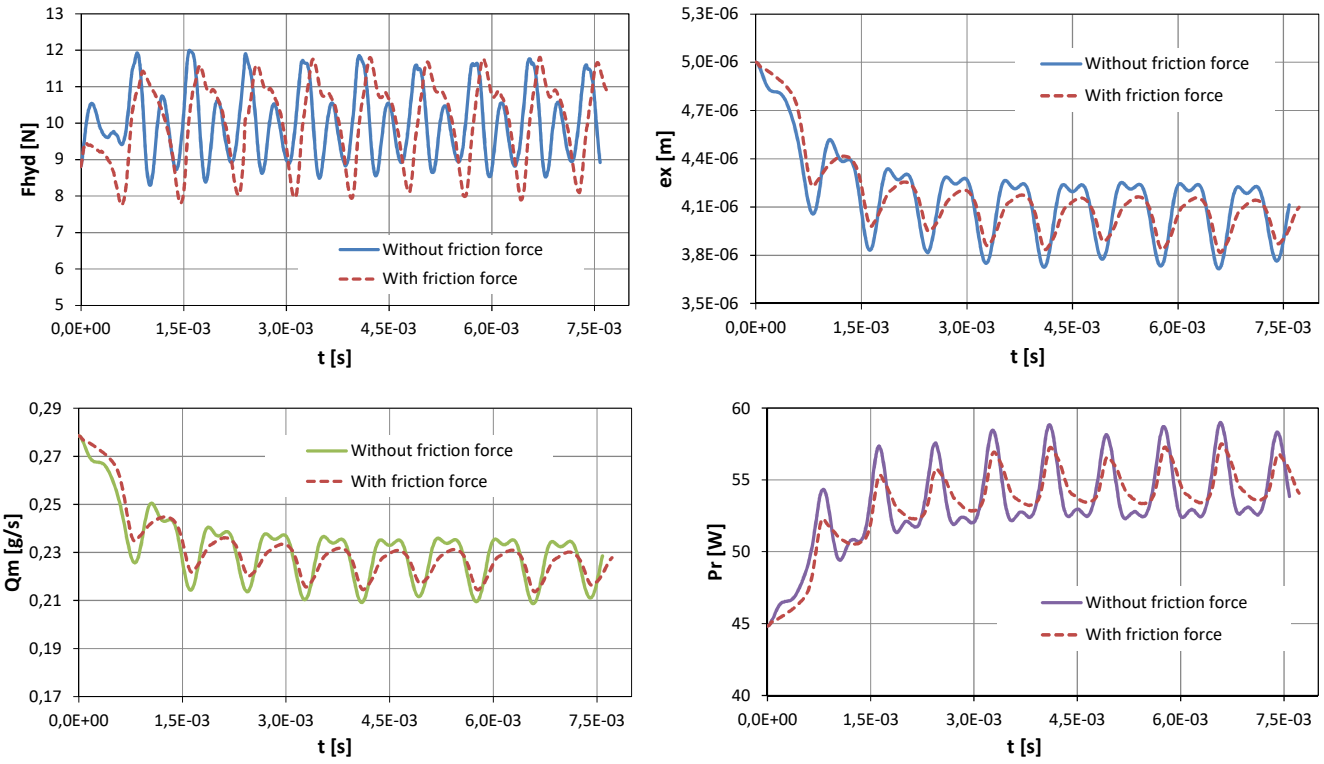

Figure 19. Results of the 1 d.o.f. dynamic analysis for $F_{X,spring} = 10N$ and $U_x = -50\ m/s$

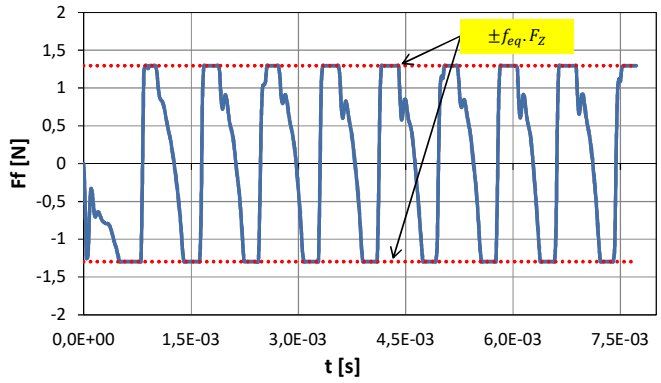

Figure 20. Variation of the nose friction force for $F_{X,spring} = 10N$ and $U_x = -50\ m/s$

The two previous calculations ($U_x = -50\ m/s$) were performed with the parameters of friction force $K_t = 1.2{\cdot}10^8\ N/m$ and $C_t = 10^{14}\ m^{-1}$.

A second set of results was obtained for lower linear speed, $U_x = -12 m/s$. For these results, the first parameter of the friction force was slightly adjusted, $K_t = 1{,}5{\cdot}10^8\ N/m$, while the second kept the same value.

Figure 21 depicts the results obtained for $F_{X,spring} = 5N$. The displacements of the segment are lower compared to the results obtained for $U_x = -50 m/s$. The average radial displacement is $e_X = 2{,}83\ \mu m$ and the amplitude is $0{,}3\ \mu m$. The average leakage mass flow rate and power loss are $Q_m = 0{,}182\ g/s$

and $\mathcal{P}_r = 4{,}5\ W$. The low impact of friction on the results is explained by the results depicted in Figure 22 showing that the displacements of the segment are mostly in the "stick" mode.

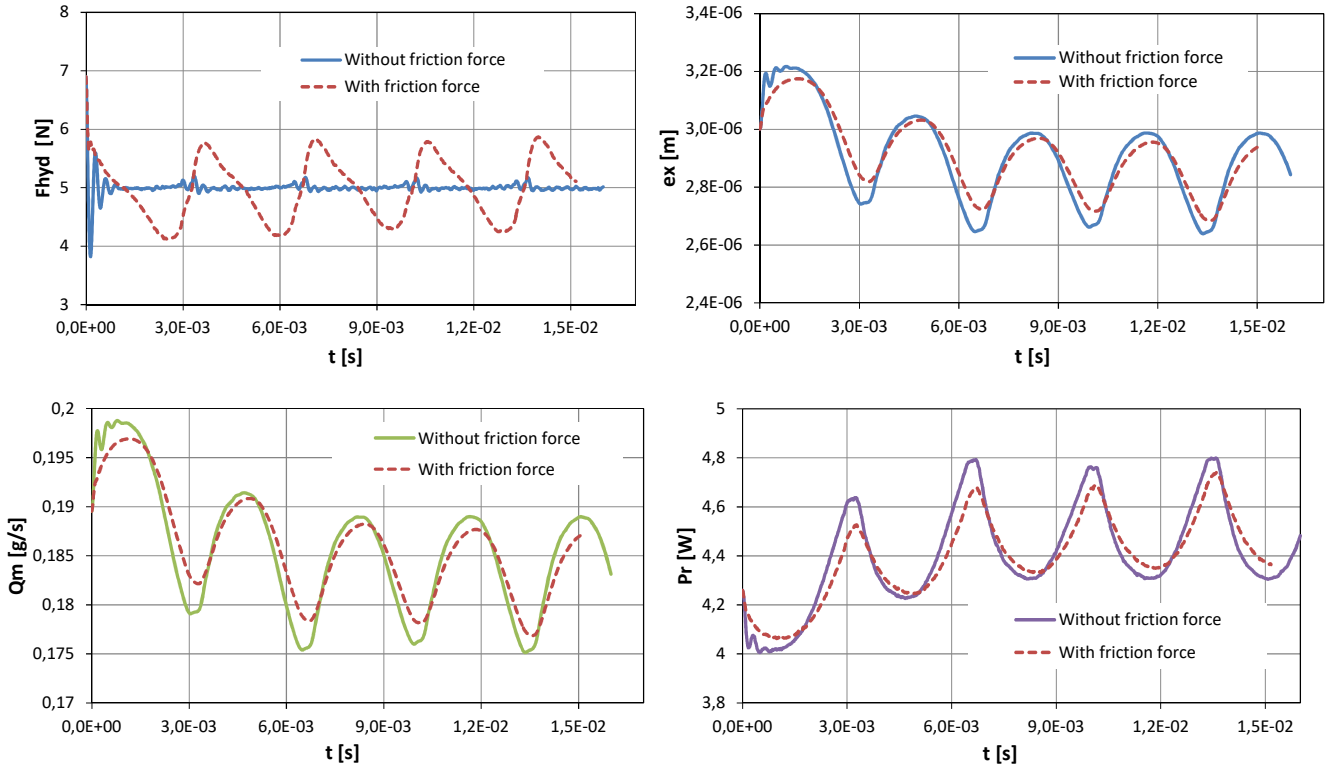

Figure 21. Results of the 1 d.o.f. dynamic analysis for $F_{X,spring} = 5N$ and $U_x = -12\ m/s$)

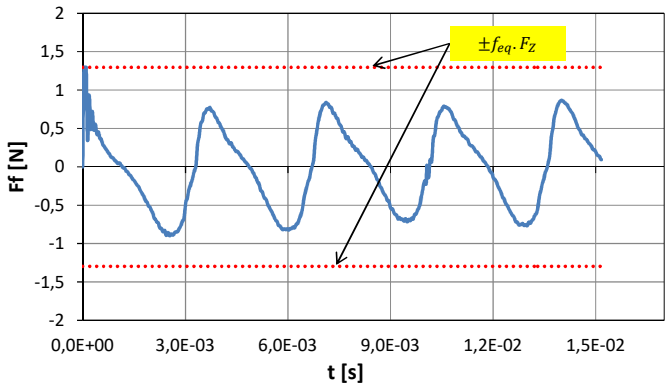

Figure 22. Variation of the nose friction force for $F_{X,spring} = 5N$ and $U_x = -12\ m/s$

When increasing the garter spring force to $F_{X,spring} = 10\ N$, the friction force is even lower. The results depicted in Figure 23 and Figure 24 show that the behavior of the segment remains similar to the previous case with a lower average radial displacement $e_X = 1{,}8\ \mu m$. The leakage mass flow rate and the average power loss of the seal are $Q_m = 0{,}146\ g/s$ and $\mathcal{P}_r = 7\ W$. The time period of motion for these last two cases is $T = 3{,}44 \cdot 10^{-3} s$.

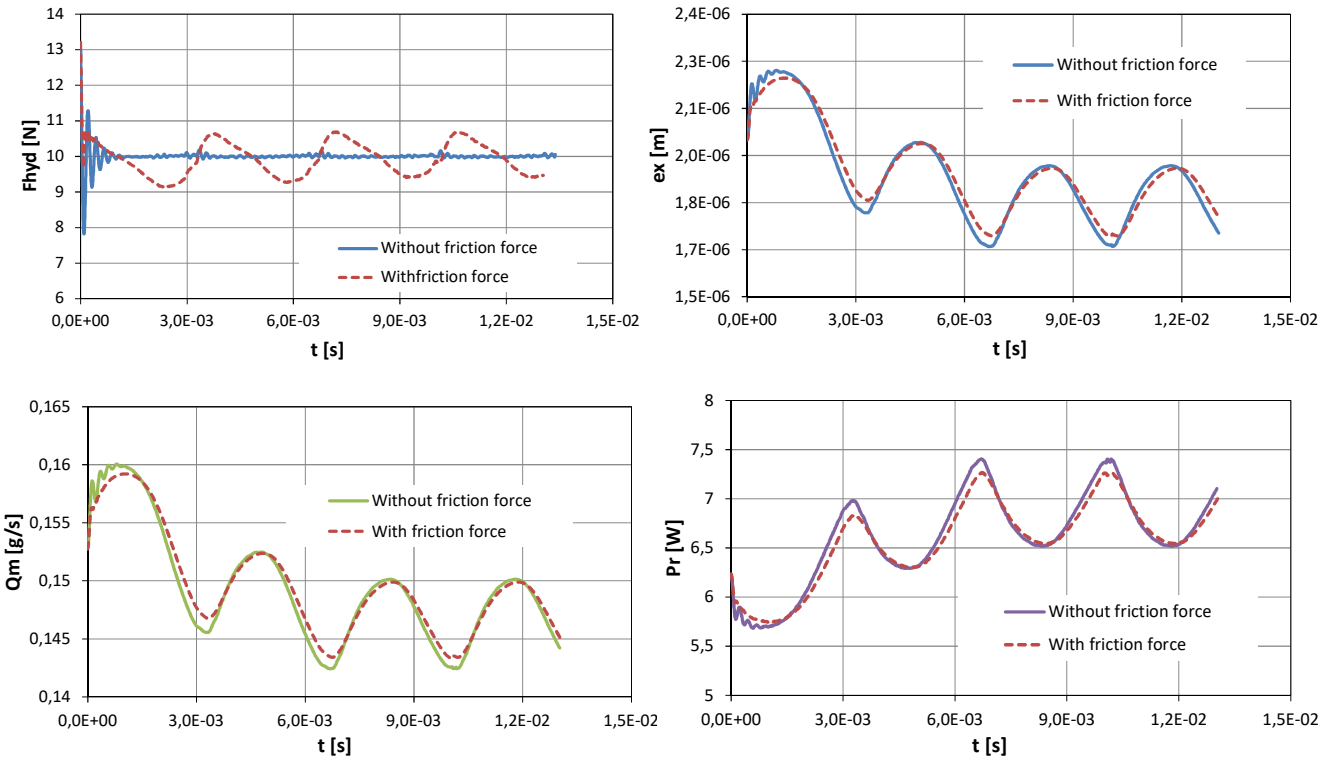

Figure 23. Results of the 1 d.o.f. dynamic analysis $F_{X,spring} = 10N$ and $U_x = -12\ m/s$

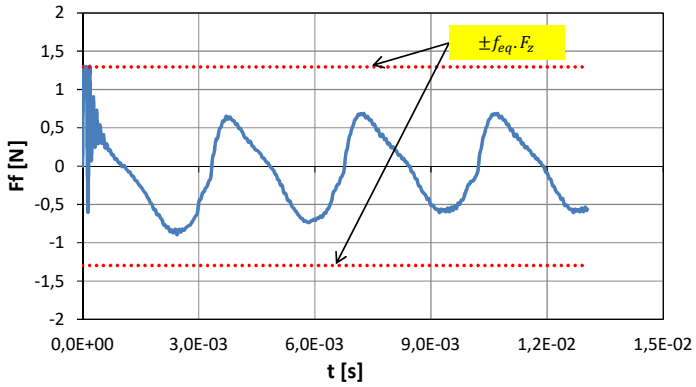

Figure 24. Variation of the nose friction force for $F_{X,spring} = 10N$ and $U_x = -12\ m/s$

The simplified approach

The calculation of the dynamic displacements of the segments might requires a computation time of the order of hours on a desktop computer. This is due to the small time step of the explicit Euler method necessary for correctly integrating the transient friction force and due to the fine grid used for modeling an important number of inclined grooves. The computational effort may appear excessive if only steady-state results such as the average leakage rate or the seal opening are sought.

A simple approach is to consider a single pattern of static grooves facing a smooth surface driven by a speed, $-U_x$. This model does not take into account the axial grooves of the segment and is therefore stationary. The domain considered will be of length $L_{xPad} = L_{xPattern}$. Figure 25 depicts the calculation domain of the simplified model. The depicted grids contain approximately 4000 triangles for the pad and 500 triangles for the lip.

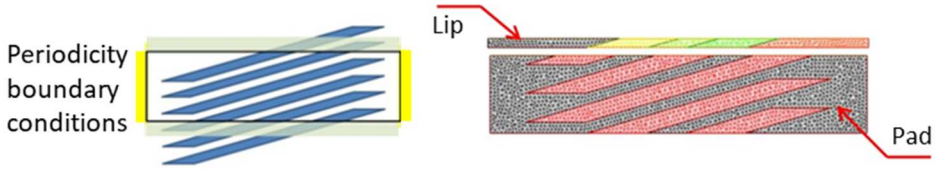

Figure 25. The calculation domain of the simplified model (boundary conditions and grid)

Figure 26 depicts the pressure field calculated for $P_{upstr} = 1.5\ bar\ P_{downstr} = 1\ bar, U_x = -50\ m/s$ and an imposed radial displacement, $e_X = 4\ \mu m$.

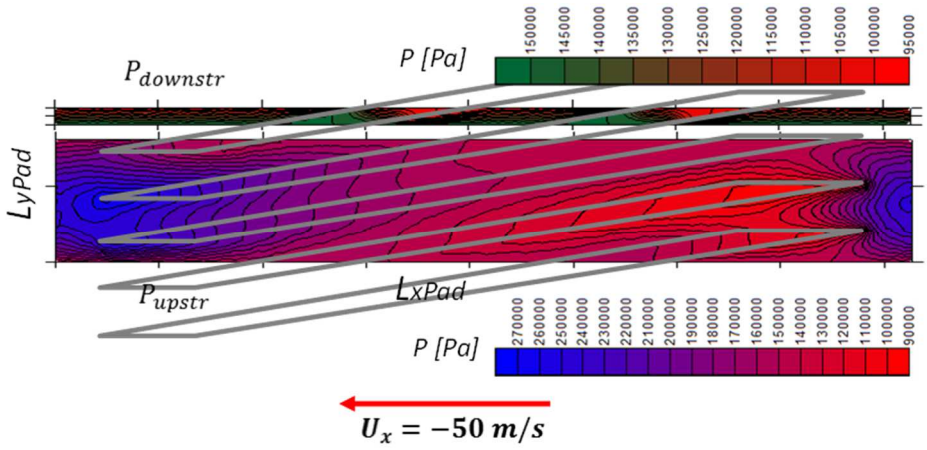

Figure 26. Pad and lip sector pressures for an imposed radial displacement $e_X = 4\ \mu m$

The low pressure zone corresponds to the leading edges of the grooves[2] inside the pad (on the right hand side of Figure 26) while a high pressure zone is located at the opposite side.

To highlight the pumping effect created by the inclined grooves and its influence on the leakage rate, calculations were made at two different upstream pressures corresponding to $\Delta P = 0.5\ bar$ and $0\ bar$ and for opposed values of the linear speed. The radial position $e_X = 4\ \mu m$ is unchanged and the results are given in Table 1.

Table 1. Values of the mass flow rate Q_m for $e_X = 4\ \mu m$

[2] The leading edge designation corresponds to the fixed reference frame where the rotor would have a positive U_x velocity.

$\boldsymbol{\Delta P}$ *[bar]*	$U_x = -50\ m/s$	$U_x = 50\ m/s$
0	$-7{,}69 \cdot 10^{-4}$ g/s	$7{,}69 \cdot 10^{-4}$ g/s
0,5	$1{,}24 \cdot 10^{-2}$ g/s	$1{,}44 \cdot 10^{-2}$ g/s

For a zero pressure difference and $U_x = -50\ m/s$, the negative value of the mass flow rate shows a leakage from downstream to upstream. This is the pumping effect induced by the orientation of the grooves. For a positive value of ΔP, the pressure gradient prevails over the pumping effect and the direction of the leakage is from upstream to downstream. However, the values of the flow rates obtained for $U_x = -50\ m/s$ remain lower than those for the reversed speed. The pumping effect therefore reduces the leakage rates.

As mentioned, the simplified approach can be applied only in the steady-state case. The friction force will therefore be constant since the "stick-slip" effects cannot be considered. Depending on the direction of the displacement of the pad towards its equilibrium position, the friction force can contribute either to the opening or to the closing of the pad. The equilibrium position will thus verify the following inequality:

$$\left|F_{hyd} - F_{X,spring}\right| \leq F_{f,nose} \tag{48}$$

Two static equilibrium positions e_{X1} and e_{X2} are obtained from this inequality (Figure 27).

$$e_{X1} : F_{hyd} = F_{X,spring} + F_{f,nose} \qquad e_{X2} : F_{hyd} = F_{X,spring} - F_{f,nose} \tag{49}$$

These equilibrium positions are solved graphically. The parameters B_e_{X1} and B_e_{X2} depicted in Figure 28 correspond to the residues of eqs. (49) for different values of e_X:

$$B\_e_{X1} = F_{hyd} - F_{X,spring} - F_{f,nose} \qquad B\_e_{X2} = F_{hyd} - F_{X,spring} + F_{f,nose} \tag{50}$$

The displacements e_{X1} and e_{X2} are the roots of equations (50).

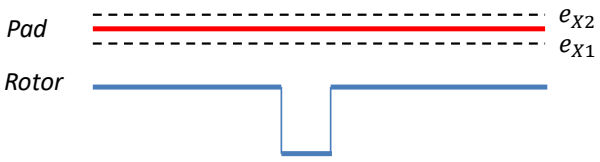

Figure 27. Equilibrium of the pad sector between two static positions, e_{X1} and e_{X2}

The results presented in Figure 28 were obtained for two values of the linear speed ($-12\ m/s$ and $-50\ m/s$) and for two values of the garter spring force, ($5\ N$ and $10\ N$). The axial spring force and the pressure difference are $F_{Z,spring} = 5N$ and $\Delta P = 0{,}5\ bar$.

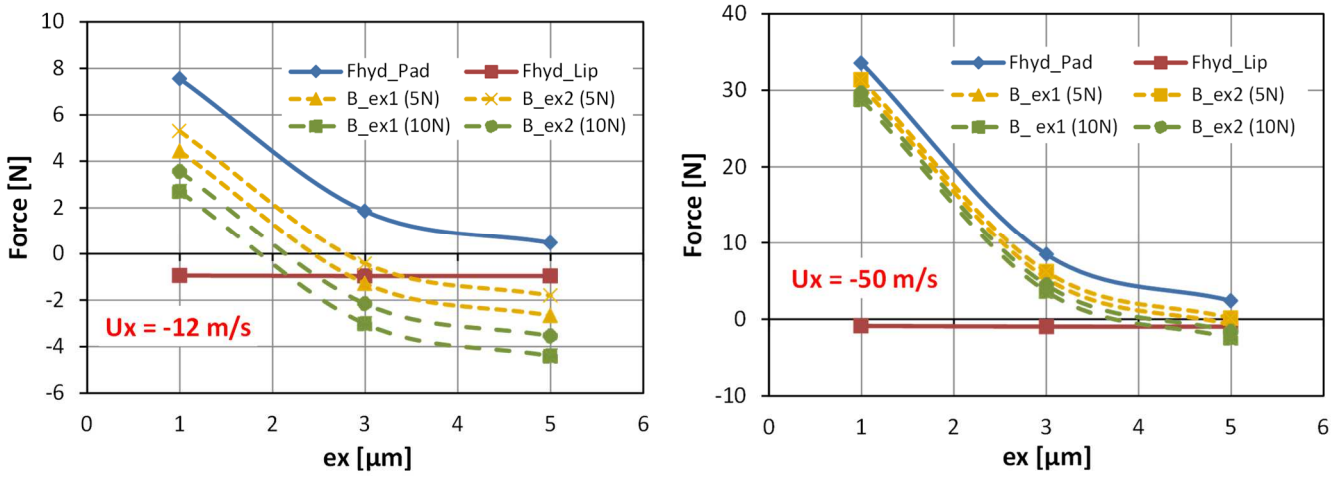

Figure 28. Radial forces and solutions of eq. (50) for $F_{g,spring} = 5\ N$ and $10\ N$ and for $U_x = -12\ m/s$ and $-50\ m/s$

The results in Figure 28a,b show two static equilibrium positions (i.e. solution of eqs. $B\_e_{X1,2} = 0$) and for each value of the garter spring forces. These resulte proove the the opening of the seal. They yield the lower and the upper limits of the radial displacement and of the leakage flow that would be expected from an unsteady simulation based on the numerical solution of the equations of motion where the Coulomb friction force on the nose would be fully considered.

A comparison of the radial displacements of the segment obtained by the simplified and the general models is presented in Table 2. The table presents the minimum, e_{X1}, and the maximum, e_{X2}, radial displacements predicted by the simplified approach as well as the average values obtained by the general model and the peak-to-peak (ptp) amplitudes with and without the nose friction force. The average values compare very well with e_{X1} and e_{X2}, i.e. they lye within these values or very close to the limits. The peak-to-peak amplitudes obtained with the general model compare also well with the difference, $\Delta e_X = e_{X2} - e_{X1}$, obtained from the simplified approach. However, discrepancies exist and they are imputable to the two parameters used in the Coulomb friction force model given by eq. (47).

Table 2. Radial displacements of the segment

		General model			Simplified model		
$F_{X,spring}$ [N]	U_x [m/s]	av. (e_X) [µm]	ptp amp. [µm]	ptp, f=0 [µm]	e_{X1} [µm]	e_{X2} [µm]	Δe_X [µm]
5	-12	2.83	0.28	0.34	2.46	2.85	0.4
10	-12	1.8	0.24	0.28	1.85	2.13	0.28
5	-50	5,3	0.2	0.6	4.73	5,3	0.57

10	-50	3.9	0.3	0.5	3.78	4.13	0.35

Summary and conclusions

This paper presents a numerical model of an annular segmented seal with rotor inclined grooves for enhancing the lift opening force. Due to the particular design of the seal, the hydrodynamic pressure field under the pad/segment is unsteady. Therefore, the segmented seal is modeled in a rotating reference frame. The analysis of a single segment is sufficient for explaining the seal opening and for estimating the leakage mass flow rate and the seal power loss. The numerical integration of the compressible Reynolds equation on a triangular grid was performed using the finite volume method and is thoroughly presented. A Newton-Raphson algorithm with a complete Jacobian matrix is first presented and proved to be particularly robust.

The radial displacement of the segment was the degree of freedom considered for explaining the seal opening. The proposed model considers the complete segment. Therefore, it is unsteady even in the rotating system and requires the time integration of the 1d.o.f. equation of motion of the segment as well as a "stick-slip" model for the nose Coulomb friction force. The computational effort can be more important and, depending on the operating conditions, the model might require triggering the numerical parameters of the Coulomb friction force.

A simplified model was therefore proposed. This second model takes into account a single pattern of inclined grooves and a limited area of the segment. Its main advantage is being steady. Moreover, it uses a constant Coulomb friction force and the computational effort is not important. The comparison of the numerical results of the two models showed that the simplified approach predicts well the radial displacement of the segment.

Nomenclature

C_t	Friction parameter [m^{-1}]
e_X	Displacement of the segment in the $\boldsymbol{X}$ direction $[m]$
$\boldsymbol{e_{x,y}}$	Unity vector in $\boldsymbol{x}, \boldsymbol{y}$ direction
F	Force $[N]$
f	Friction coefficient of the segment
h	Thin film thickness $[m]$
h_{groove}	Groove depth $[m]$
K_t	Friction parameter $[N\ m^{-1}]$
L_x, L_y	Length and width $[m]$
l_{ij}	Distance between two point i and j $[m]$
$\dot{m}$	Elementary mass flow rate $[Kg\ m^{-1}\ s^{-1}]$
$\boldsymbol{n}$	Normal outgoing vector
$n_{pattern}$	Number of rotor patterns
P	Pressure $[Pa]$

$\tilde{P}$	Upwinded Pressure $[Pa]$
$\mathcal{P}_r$	Power loss $[W]$
Q_m	Leakage mass flow rate $[g/s]$
R	Residue
$\mathcal{R}$	Ideal gas constant $[J\ Kg^{-1}K^{-1}]$
S	Surface $[m^2]$
T	Temperature $[K]$
t	Time coordinate [s]
U_x	Rotor linear speed in the direction $\boldsymbol{x}$ $[m/s]$
V_n	Fluid linear speeds in the direction $\boldsymbol{n}$ $[m/s]$
x, y, z	Cartesian coordinates $[m]$

ΔP	Pressure difference $[bar]$
Δt	Time step $[s]$
θ	Angular coordinate $[1]$
θ_P	Half amplitude of the pad $[1]$
θ_s	Half amplitude of the segment $[1]$
μ	Dynamic viscosity $[Pa.s]$
ρ	Density $[kg/m^3]$
Ω	Rotation speed $[1\ /s]$
γ	Length of an edge $[m]$
$\boldsymbol{\xi_{ij}}$	Unity vector between two points i and j
Λ	Compressibility number

References

[1] Chupp R., Hendricks R., Lattime S., Steinetz B., 2006, «Sealing in Turbomachinery» Journal of Propulsion and Power, vol. 22(2), pp 313-349.

[2] Flitney R., 2014, *Rotary Seals, Seals and Sealing Handbook (6th edition)*, pp. 105-288, Butterworth-Heinemann, Elsevier.

[3] Burcham, R.E., 1978, "Liquid Rocket Engine Turbopump Rotating-Shaft Seal ", NASA S-8121.

[4] Burcham, R.E., 1983, "High-Speed Cryogenic Self-Acting Shaft Seals for Liquid Rocket Turbopumps", NASA CR-168194.

[5] Garrison G.M., 2011, «Hydrodynamic circumferential seal system for large translations » Publication of US 8 091 89 8 B2.

[6] Oike, M., Nosaka, M., Watanabe, Y., Kikuchi, M., Kamijo, K., 1987, "Experimental Study on High-Pressure Gas Seals for a Liquid Oxygen Turbopump", STLE Transactions 31(1), 91-97.

[7] Oike, M., Nosaka, M., Kikuchi, M., Watanabe, Y., Kamijo, K., 1990, "Study on a Carbon Segmented Circumferebtial Seal for a Liquid Oxygen Turbopump" Proceedings of the Japan International Tribology Conference, Nagoya, 283-288.

[8] Nosaka, M., Oike, M., 1990, "Shaft Seals of Turbopumps for Rockets ", Japanese Journal of Tribology, 35(4), 411-421.

[9] Oike, M., Nosaka, M., Kikuchi, M., Watanabe, Y., 1992, “Performance of a Segmented Circumferential Seal for a Liquid Oxygen Turbopump (Part 1): Sealing Performance“, Japanese Journal of Tribology, 37(4), 511-523.

[10] Oike, M., Nagao, R., Nosaka, M., Kamijo, K., Jinnouchi, T. 1995, “Characteristics of a Shaft Seal System for the LE-7 Liquid Oxygen Turbopump “, AIAA 95-3102.

[11] Arghir, M., Mariot, A., 2017, “Theoretical Analysis Of The Static Characteristics Of The Carbon Segmented Seal”, ASME Journal of Tribology, Vol. 139 (6): 062202.

[12] Arghir, M., Dahite, S., 2019, “Numerical Analysis of Lift Generation in A Radial Segmented Gas Seal” GT2019-90492, ASME Turbo Expo, Phoenix (AZ).

[13] Dahite, S., 2020, « Etude sur le fonctionnement du joint radial segmenté pour une application turbomachine », Thèse de Doctorat de l’Université de Poitiers.

[14] Dahite, S., Arghir M., 2020, “Thermogasodynamic Analysis of the Segmented Annular Seal”, ASME Journal of Tribology, doi:10.1115/1.4048727.

[15] Whipple, R. T. P., 1949, «Herringbone Pattern Thrust Bearing», Atomic Energy Research Establishment, Harwell, Berkshire, England, T/M29.

[16] Hsing, F. C., 1972, «Formulation of a Generalized Narrow Groove Theory for Spiral Grooved Viscous Pumps» Journal of Lubrication Technology, Trans. ASME, vol. 94(1), p. 81-85.

[17] Smalley, A. J., 1972, «The Narrow Groove Theory of Spiral Grooved Gas Bearings: Development and Application of a Generalized Formulation for Numerical Solution» Journal of Lubrication Technology, Trans. ASME, vol. 94(1), p. 86-92.

[18] Castelli, V., Vohr, J., 1967, «Performance Characteristics of Herring Bone-Grooved Journal Bearing Operating at High Eccentricity Ratios and with Misalignment» NASA MTI-67TR15.

[19] Constantinescu, V. N., Castelli V., 1969, « On the local Compressibility Effect in Spiral-Groove Bearings» Journal of Lubrication Technology, Trans. ASME, vol. 91(1), pp. 76-86.

[20] Yu Y., Pu G., Jian K., 2017, «Modeling and analysis of the static characteristics and dynamic responses of Herringbone-grooved Thrust Bearings» IOP Conference Series: Materials Science and Engineering, vol. 280.

[21] Guenat, E., Schiffmann, J, 2020, « Dynamic force coefficients identification of air-lubricated Herringbone Grooved Journal Bearing » Mechanical Systems and Signal Processing, vol. 136 , 106498. and Signal Processing 136, 106498. doi:10.1016/j.ymssp.2019.106498

[22] Wildman M., 1968, «On the behavior of Grooved Plate Thrust Bearings with Compressible Lubricant» Journal of Lubrication Technology, Trans. ASME, vol. 90(1), pp. 226-232.

[23] Bonneau D., Huitric J., Tournerie B., 1993, «Finite Element Analysis of Grooved Gas Thrust Bearings and Grooved Gas Face Seals » Journal of Tribology, Trans. ASME, vol. 115(3), pp. 348-354.

[24] Bonneau D., Absi J., 1994, «Analysis of Aerodynamic Journal Bearings with Small Number of Herringbone Grooves by Finite Element Method» Journal of Tribology, Trans. ASME, vol. 116(4), pp.698-704.

[25] Zirkelback N., San Andrès L., 1998, «Finite Element Analysis of Herringbone Groove Journal Bearings: A parametric Study» Journal of Tribology, Trans. ASME, vol. 120(2), pp.234-240.

[26] Lehn A., Schweizer B., 2016, «Generalized Reynolds equation for fluid film problems with arbitrary boundary conditions: application to double-sided spiral groove thrust bearing» Archive of Applied Mechanics, vol. (86), pp. 743-760.

[27] Hecht F., 2012, «New development in FreeFem++» Journal of Numerical Mathematics, vol. 20, pp. 251-266.

[28] Schenk, O., Gartner, K., 2004, «Solving Unsymmetric Sparse Systems of Linear Equations with PARDISO», Journal of Future Generation Computer Systems, vol. 20(3), pp. 475-487.

[29] Wriggers, P., 2006, *Computational Contact Mechanics*, Springer-Verlag Berlin Heidelberg.

Appendix

$$\frac{\partial R(P)}{\partial P_i} = (a_i + \bar{a}_i) + \left(\frac{\partial a_i}{\partial P_i} + \frac{\partial \bar{a}_i}{\partial P_i}\right) P_i - \left(\frac{\partial a_0}{\partial P_i} + \frac{\partial \bar{a}_0}{\partial P_i}\right) P_0 - \frac{\partial b_0}{\partial P_i} + \sum_{j_{B_i}=1\backslash\{i\}}^{n_{B_i}} \frac{\partial \bar{a}_{j_{B_i}}}{\partial P_i} P_{j_{B_i}} - \sum_{j_{A_i}=1\backslash\{i\}}^{n_{A_i}} \frac{\partial \bar{a}_{j_{A_i}}}{\partial P_i} P_{j_{A_i}} \quad (51)$$

$$\frac{\partial R(P)}{\partial P_0} = \sum_{i=1}^{3} \left(\frac{\partial a_i}{\partial P_0} + \frac{\partial \bar{a}_i}{\partial P_0}\right) P_i - \left(\frac{\partial a_0}{\partial P_i} + \frac{\partial \bar{a}_0}{\partial P_i}\right) P_0 - (a_0 + \bar{a}_0) - \frac{\partial b_0}{\partial P_0} + \sum_{j_{B_i}=1\backslash\{i\}}^{n_{B_i}} \frac{\partial \bar{a}_{j_{B_i}}}{\partial P_0} P_{j_{B_i}} - \sum_{j_{A_i}=1\backslash\{i\}}^{n_{A_i}} \frac{\partial \bar{a}_{j_{A_i}}}{\partial P_0} P_{j_{A_i}} \quad (52)$$

$$\frac{\partial R(P)}{\partial P_{j_{B_i}}} = \bar{a}_{j_{B_i}} \quad (53)$$

$$\frac{\partial R(P)}{\partial P_{j_{A_i}}} = -\bar{a}_{j_{A_i}} \quad (54)$$

With :

$$\frac{\partial a_i}{\partial P_i} = \frac{\partial a_0}{\partial P_i} = (1 - \delta_i)\beta_i \quad (55)$$

$$\frac{\partial a_i}{\partial P_0} = \delta_i \beta_i \quad (56)$$

$$\frac{\partial a_0}{\partial P_0} = \sum_{j=1}^{3} \frac{\partial a_j}{\partial P_0} \quad (57)$$

$$\frac{\partial \bar{a}_i}{\partial P_i} = \frac{\partial \bar{a}_0}{\partial P_i} = \frac{\partial \varphi_i}{\partial P_i} S^i \left(\frac{1}{\sum_{k_{B_i}=0}^{n_{B_i}} S_{k_{B_i}}} - \frac{1}{\sum_{k_{A_i}=0}^{n_{A_i}} S_{k_{A_i}}} \right) \tag{58}$$

$$\frac{\partial \bar{a}_i}{\partial P_0} = \frac{\partial \varphi_i}{\partial P_0} S^i \left(\frac{1}{\sum_{k_{B_i}=0}^{n_{B_i}} S_{k_{B_i}}} - \frac{1}{\sum_{k_{A_i}=0}^{n_{A_i}} S_{k_{A_i}}} \right) \tag{59}$$

$$\frac{\partial \bar{a}_0}{\partial P_0} = \sum_{i=1}^{3} \frac{\partial \varphi_i}{\partial P_0} S^0 \left(\frac{1}{\sum_{k_{B_i}=0}^{n_{B_i}} S_{k_{B_i}}} - \frac{1}{\sum_{k_{A_i}=0}^{n_{A_i}} S_{k_{A_i}}} \right) \tag{60}$$

$$\frac{\partial \bar{a}_{j_{B_i}}}{\partial P_i} = \frac{\partial \varphi_i}{\partial P_i} \frac{S_{j_{B_i}}}{\sum_{k_{B_i}=0}^{n_{B_i}} S_{k_{B_i}}} \tag{61}$$

$$\frac{\partial \bar{a}_{j_{A_i}}}{\partial P_i} = \frac{\partial \varphi_i}{\partial P_i} \frac{S_{j_{A_i}}}{\sum_{k_{A_i}=0}^{n_{A_i}} S_{k_{A_i}}} \tag{62}$$

$$\frac{\partial \bar{a}_{j_{B_i}}}{\partial P_0} = \frac{\partial \varphi_i}{\partial P_0} \frac{S_{j_{B_i}}}{\sum_{k_{B_i}=0}^{n_{B_i}} S_{k_{B_i}}} \tag{63}$$

$$\frac{\partial \bar{a}_{j_{A_i}}}{\partial P_0} = \frac{\partial \varphi_i}{\partial P_0} \frac{S_{j_{A_i}}}{\sum_{k_{A_i}=0}^{n_{A_i}} S_{k_{A_i}}} \tag{64}$$

where :

$$\frac{\partial \varphi_i}{\partial P_i} = (1-\delta_i) \frac{{h_{0i}}^3}{12\mu} \tan\left(\vec{n}_i, \vec{\xi}_i\right) \left[1 + \frac{1}{l_{0c_i} \cos\left(\vec{n}_i, \vec{\xi}_i\right)} \frac{{h_{ii}}^3 - {h_{0i}}^3}{12\mu(C_{ii} + C_{0i})} \right] \tag{65}$$

$$\frac{\partial \varphi_i}{\partial P_0} = \delta_i \frac{{h_{0i}}^3}{12\mu} \tan\left(\vec{n}_i, \vec{\xi}_i\right) \left[1 + \frac{1}{l_{0c_i} \cos\left(\vec{n}_i, \vec{\xi}_i\right)} \frac{{h_{ii}}^3 - {h_{0i}}^3}{12\mu(C_{ii} + C_{0i})} \right] \tag{66}$$

and :

$$\frac{\partial b_0}{\partial P_i} = (1-\delta_i) \frac{h_{0i}}{2} U_x \gamma_i \cos\alpha_i - (1-\delta_i) \frac{{h_{0i}}^3}{12\mu} \gamma_i \frac{h_{0i} - h_{ii}}{2(C_{ii} + C_{0i})} \frac{U_x \cos\alpha_i}{l_{0c_i} \cos\left(\vec{n}_i, \vec{\xi}_i\right)} \tag{67}$$

$$\frac{\partial b_0}{\partial P_0} = \sum_{i=1}^{3} \delta_i \frac{h_{0i}}{2} U_x \gamma_i \cos\alpha_i - \sum_{i=1}^{3} \delta_i \frac{{h_{0i}}^3}{12\mu} \gamma_i \frac{h_{0i} - h_{ii}}{2(C_{ii} + C_{0i})} \frac{U_x \cos\alpha_i}{l_{0c_i} \cos\left(\vec{n}_i, \vec{\xi}_i\right)} \tag{68}$$